JACS
JOURNAL OF THE AMERICAN CHEMICAL SOCIETY
Article
pubs.acs.org/JACS

# Redox-Active Scandium Oxide Cluster inside a Fullerene Cage: Spectroscopic, Voltammetric, Electron Spin Resonance Spectroelectrochemical, and Extended Density Functional Theory Study of $Sc_4O_2@C_{80}$ and Its Ion Radicals

Alexey A. Popov,*[,†,‡] Ning Chen,[§,#] Julio R. Pinzón,[∥,▽] Steven Stevenson,*[,⊥] Luis A. Echegoyen,*[,§] and Lothar Dunsch*[,†]

[†]Leibniz-Institute for Solid State and Materials Research, Department of Electrochemistry and Conducting Polymers, 01069 Dresden, Germany

[‡]Chemistry Department, Moscow State University, 119992 Moscow, Russian Federation

[§]Department of Chemistry, University of Texas at El Paso, El Paso, Texas 79968-0519, United States

[∥]Department of Chemistry, Clemson University, Clemson, South Carolina 29634-0973, United States

[⊥]Department of Chemistry, Indiana-Purdue University at Fort Wayne, Fort Wayne, Indiana 46895-1499, United States

Supporting Information

**ABSTRACT:** The clusterfullerene $Sc_4O_2@C_{80}$ with a mixed redox state of scandium was found to be an exciting molecule for endohedral electrochemistry as demonstrated by means of an in situ electron spin resonance (ESR) spectroelectrochemical study of the spin density distribution in its electrochemically generated cation and anion radicals. The compound exhibits two reversible reduction and oxidation steps with a relatively small electrochemical gap of 1.10 V. The ESR spectra of the ion radicals have a rich hyperfine structure caused by two pairs of equivalent Sc atoms. The Sc-based hyperfine structure with large hyperfine coupling constants shows that both oxidation and reduction of $Sc_4O_2@C_{80}$ are in cavea redox processes, which is the subject of endohedral electrochemistry. The assignment of the experimentally determined $a(^{45}Sc)$ values to the two types of Sc atoms in the $Sc_4O_2$ cluster was accomplished by extended density functional theory and molecular dynamics simulations. Sc atoms adopting a divalent state in the neutral $Sc_4O_2@C_{80}$ exhibited an especially large coupling constant of 150.4 G in the cation radical, which is the record high $a(^{45}Sc)$ value for Sc-based endohedral metallofullerenes. Such a high value is explained by the nature of the highest occupied molecular orbital (HOMO) localized on the six-atom $Sc_4O_2$ cluster. This HOMO is a Sc−Sc bonding MO and hence has large contributions from the 4s atomic orbitals of $Sc^{II}$. We claim that ESR spectroelectrochemistry is an invaluable experimental tool in the studies of metal−metal bonding in endohedral metallofullerenes and in endohedral electrochemistry.

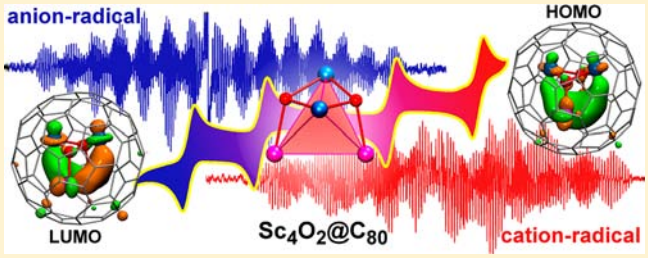


## INTRODUCTION

Endohedral metallofullerenes (EMFs) known so far are able to encapsulate up to four metal atoms.[1−6] The electron transfer from the endohedral metal atoms to the carbon cage results in the positive charge of the former and therefore in the strong Coulomb repulsion between the positively charged ions trapped in the inner space of the EMF. Repulsive metal−metal interactions in EMFs can be compensated by attractive interactions between the metal ions and the negatively charged nonmetal atoms,[7] and therefore, the vast majority of EMFs with two or more metal atoms are clusterfullerenes such as $M_3N@C_{2n}$ (M = Sc, Y, lanthanides),[3,4,8−17] $Sc_3CH@C_{80}$,[18] $M_{2−4}C_2@C_{2n}$,[19−25] $Sc_3NC@C_{78,80}$,[26,27] $Sc_4O_{2,3}@C_{80}$,[28,29] or $M_2S@C_{2n}$.[30,31] In particular, the cluster of four Sc atoms inside a $C_{80}$ cage can be stabilized by two[28] or three[29] oxygen atoms or by a carbide unit.[25] A single-crystal X-ray diffraction study of $Sc_4O_2@C_{80}$ revealed that Sc atoms form a tetrahedral cluster, while two $\mu^3$-coordinated oxygen atoms are located above the centers of two faces of the $Sc_4$ tetrahedron (Figure 1).[28] The studies of the electronic structure of $Sc_4O_2@C_{80}$[7,32,33] showed that Sc atoms are in the mixed valence state, and the formal charge distribution in the molecule can be described as $(Sc^{2+})_2(Sc^{3+})_2(\mu^3\text{-}O^{2−})_2@C_{80}^{6−}$. In particular, the Sc atoms bonded to two oxygen atoms at once are in the trivalent state ($Sc^{III}$ hereafter), whereas two other Sc atoms (each bonded to only one oxygen atom) are in the divalent state ($Sc^{II}$) and form a Sc−Sc bond. Both the highest occupied molecular orbital (HOMO) and lowest unoccupied molecular orbital (LUMO) of $Sc_4O_2@C_{80}$ are localized on the endohedral cluster (Figure

Received: July 10, 2012
Published: August 27, 2012

   dx.doi.org/10.1021/ja306728p | J. Am. Chem. Soc. 2012, 134, 19607−19618

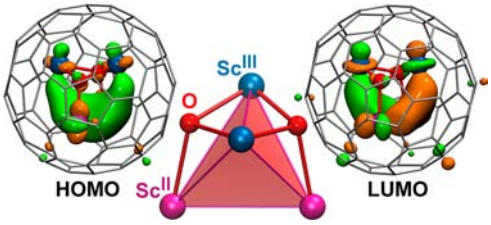


**Figure 1.** HOMO and LUMO of $Sc_4O_2@C_{80}$ and enlarged figure of the $Sc_4O_2$ cluster with the indication of the atom types. For clarity, $Sc^{II}$ and $Sc^{III}$ are plotted in different colors.

1), and the HOMO can be described as essentially a $Sc^{II}$–$Sc^{II}$ bonding MO, albeit with some contribution from $Sc^{III}$ atoms.

Recently, we have established that the unique ability of the carbon cages to stabilize unusual metal clusters can be extended to manipulation of the electronic and spin states of the endohedral species by means of endohedral (in cavea) redox reactions, which is the main subject of endohedral electrochemistry.[34−36] This term defines a special situation found in some EMFs, whose carbon cage remains "transparent" in the process of the electron transfer for the electron, and hence, the redox process affects the endohedral species rather than the carbon cage. The list of EMFs with well-established endohedral redox reactions includes $La_2@C_{80}$ (reduction),[37] $Sc_3N@C_{80}$ (reduction),[38] $CeLu_2N@C_{80}$ (oxidation of Ce),[36] $TiM_2N@C_{80}$ (M = Sc,[35] Y;[39] both reduction and oxidation of Ti), and some other clusterfullerenes and dimetallofullerenes (see ref 34 for a review). A prerequisite for the EMF molecule to exhibit an in cavea redox process is the endohedral localization of its frontier molecular orbitals. Experimentally, the endohedral electron transfer can be identified by a shift of the redox potential from the values in the analogue EMFs with fullerene-based redox process, but the unambiguous proof of the endohedral redox process can be obtained by means of electron spin resonance (ESR) spectroelectrochemistry. When an EMF molecule is reduced or oxidized in the single-electron transfer reaction, the resulting change of its spin state is in principle detectable by ESR spectroscopy, whereas the localization of the spin density on the metal atoms results in the hyperfine structure of the ESR signal with large hyperfine coupling (hfc) constants and a characteristic shift of the *g* factor from the free-electron value ($g$ = 2.0023).

The unprecedented electronic structure of the endohedral cluster in $Sc_4O_2@C_{80}$ predicted by theory[7,32,33] calls for its verification via extended experimental studies. The endohedral localization of the frontier MOs (Figure 1) indicates that $Sc_4O_2@C_{80}$ can exhibit an endohedral electron transfer in both the reduction and oxidation processes. A nuclear spin $I(^{45}Sc)$ = 7/2 of the sole natural isotope of Sc makes it suitable for an analysis of the hyperfine structure in the ESR spectra of the cation and anion radicals. In this work, we report on the detailed electrochemical and ESR spectroelectrochemical studies of $Sc_4O_2@C_{80}$. The paper is organized as follows: First, we give a spectroscopic characterization of $Sc_4O_2@C_{80}$ by NMR and vibrational spectroscopies. Then we discuss the redox properties of $Sc_4O_2@C_{80}$, Finally, the main part of the paper is devoted to the analysis of the ESR spectra and their interpretation by means of density functional theory (DFT) and molecular dynamics.

## RESULTS AND DISCUSSION

**NMR Spectra.** The $^{13}C$ NMR spectrum of $Sc_4O_2@C_{80}$ (Figure 2) shows two sharp peaks at 137.29 and 144.82 ppm in

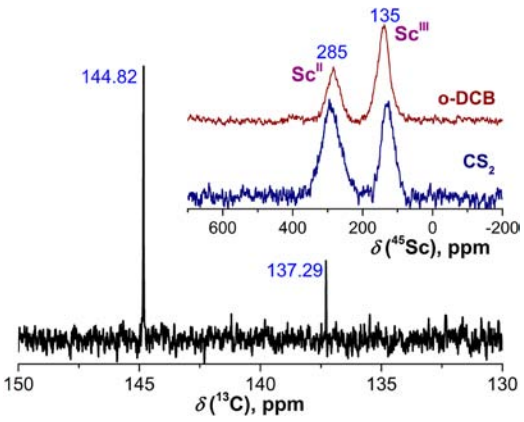


**Figure 2.** $^{13}C$ and $^{45}Sc$ NMR spectra of $Sc_4O_2@C_{80}$.

a 1:3 ratio, indicating that the $Sc_4O_2$ cluster is rotating freely inside the $C_{80}$-$I_h(7)$ cage on the time scale of NMR spectroscopy. These values are only slightly different from the signals at 136.87 and 144.18 ppm measured for $Sc_3N@C_{80}$-$I_h(7)$ at the same conditions.[40]

The $^{45}Sc$ NMR spectrum of $Sc_4O_2@C_{80}$ exhibits two peaks at 129/138 and 292/285 ppm in $CS_2$/*o*-DCB. This proves that the cluster is rather rigid and that oxygen atoms do not rearrange between different faces of the $Sc_4$ tetrahedron (which would result in the coalescence of the two Sc signals). Two different $^{45}Sc$ signals were observed at room temperature for $Sc_3CN@C_{80}$, $Sc_2C_2@C_{82}$-$C_s(6)$,[41,42] and $Sc_2C_2@C_{80}$-$C_{2v}(5)$[43] (for the latter two compounds, a higher temperature resulted in coalescence of Sc signals at higher temperatures).

As mentioned in the Introduction, $Sc_4O_2$ has two pairs of Sc atoms in $Sc^{II}$ and $Sc^{III}$ valence states. It might be anticipated that the divalent Sc atoms are more shielded because of the higher electron density, whereas the low-field signal at ∼290 ppm might be assigned to $Sc^{III}$. Counterintuitively, DFT calculations show that the signal with the larger chemical shift should be assigned to $Sc^{II}$ (see the Supporting Information for computed values). In agreement with the experimental data, DFT predicted that the difference between the chemical shifts of $Sc^{II}$ and $Sc^{III}$ is in the range of 110−210 ppm (the values vary strongly depending on the cluster orientation with respect to the cage; see Table S2 in the Supporting Information).

In Ramsey's theory for nuclear magnetic shielding,[44] the components of the shielding tensor evolve as a sum of two terms: (i) the diamagnetic term, which arises from the unperturbed ground-state wave function, and (ii) the paramagnetic term, which describes the currents induced by excitations of the ground-state wave function by the magnetic field perturbation. Since the diamagnetic term is highly transferable for the majority of chemical elements (except for hydrogen), the variation of the chemical shifts of Sc is to be attributed to the paramagnetic term. The latter can be expressed as a double sum over occupied and virtual MOs. Each member of the sum includes the excitation energy (roughly corresponding to the energy difference of the occupied and virtual molecular orbitals) in the denominator. The nominator is a product of an angular momentum operator with the local angular momentum operator acting around the


dx.doi.org/10.1021/ja306728p | J. Am. Chem. Soc. 2012, 134, 19607−19618

nuclei of interest and hence ensures the local character of the term. Since the HOMO of $Sc_4O_2@C_{80}$ is largely a $Sc^{II}$-based MO and LUMO of the molecule with equal contributions from $Sc^{II}$ and $Sc^{III}$, the paramagnetic term for $Sc^{II}$ is expected to be higher than that of $Sc^{III}$.

So far there has been only one report on the $^{45}Sc$ NMR spectrum of $Sc^{II}$ in EMFs. Aakasaka et al. found that the $\delta(^{45}Sc^{II})$ value in $Sc_2@C_{82}$ is 430 ppm.[45] The $\delta(^{45}Sc^{II})$ value in $Sc_4O_2@C_{80}$ is shifted upfield by ca. 140 ppm. These data also agree well with our DFT calculations showing that $Sc^{II}$ in $Sc_2@C_{82}$ is less shielded than in $Sc_4O_2@C_{80}$ by 140−270 ppm (see Table S2 in the Supporting Information).

The $\delta(^{45}Sc^{III})$ values in Sc-based EMFs vary in a very broad range from 90 ppm in $Sc_3N@C_{68}$[9] to ca. 360 ppm in $Sc_3NC@C_{80}$[27] (see Table 1). The $^{45}Sc^{III}$ chemical shift in $Sc_4O_3@C_{80}$ is close to the lowest limits for $Sc^{III}$ in EMFs reported so far.[9,43] Compared to that in $Sc_3N@C_{80}$-$I_h$(7) (200 ppm), the $\delta(^{45}Sc^{III})$ value in $Sc_4O_2@C_{80}$ is 70 ppm upfield, which agrees with the DFT-predicted difference of 60−120 ppm (see Table S2 in the Supporting Information).

**Table 1. $^{45}Sc$ NMR Chemical Shifts (ppm) in Different Sc-Based EMFs**

| | $\delta(Sc^{II})$ | $\delta(Sc^{III})$ | ref |
|---|---|---|---|
| $Sc_4O_2@C_{80}$-$I_h$(7) | 292/285[a] | 129/138[a] | this work |
| $Sc_2@C_{82}$-$C_{3v}$(8) | 430 | | 45 |
| $Sc_2C_2@C_{80}$-$C_{2v}$(5) | | 130/170,[b] 150 (HT[c]) | 43 |
| $Sc_2C_2@C_{82}$-$C_s$(6) | | 200/245,[b] 220 (HT[c]) | 41, 42 |
| $Sc_2C_2@C_{82}$-$C_{3v}$(8) | | 225 | 41 |
| $Sc_3N@C_{68}$-$D_3$(6140) | | 90[b] | 9 |
| $Sc_3N@C_{80}$-$I_h$(7) | | 200 | 8 |
| $Sc_3N@C_{80}$-$D_{5h}$(6) | | 212 | 46 |
| $Sc_3NC@C_{80}$ | | 280/360[b] | 27 |
| $Sc_2S@C_{82}$-$C_{3v}$(8) | | 290 | 30 |
| $Sc_2S@C_{72}$-$C_s$(10528) | | 183 | 47 |

[a]Values measured in $CS_2$/$o$-DCB. [b]Exact values were not given and are estimated from the figures in the original papers. [c]Values measured at higher temperatures (>400 K) after coalescence of two signals.

The broad range covered by the $\delta(^{45}Sc)$ values depending on the valence state and cage/cluster structure of the Sc-based EMFs shows that $^{45}Sc$ NMR spectroscopy can be an important and sensitive probe of the valence state of Sc atoms in EMFs.

**Vibrational Spectra.** Figure 3 compares the IR spectra of $Sc_4O_2@C_{80}$ to the spectrum of another clusterfullerene with a $C_{80}$-$I_h$(7) carbon cage, $Sc_3N@C_{80}$. The computed spectrum of $Sc_4O_2@C_{80}$ agrees well with the experimental data and thus can serve as a guide for an assignment discussed below. In the frequency range of tangential vibrations of the carbon cage (1000−1600 $cm^{-1}$), the spectra of $Sc_4O_2@C_{80}$ and $Sc_3N@C_{80}$ are rather similar; however, the wave numbers of corresponding peaks in $Sc_4O_2@C_{80}$ are slightly red-shifted. The softening of the cage modes points to a somewhat larger negative charge on the fullerene in the oxide clusterfullerene in comparison to that in $Sc_3N@C_{80}$. At lower frequencies, the spectra of the two compounds are distinctly different. The group of medium-intensity peaks at 650−800 $cm^{-1}$ in the spectrum of $Sc_4O_2@C_{80}$ has no counterpart in the spectrum of $Sc_3N@C_{80}$.[48] According to DFT calculations, these peaks correspond to radial cage modes, and their absence (more correct, low intensity) in the spectrum of $Sc_3N@C_{80}$ indicates that the

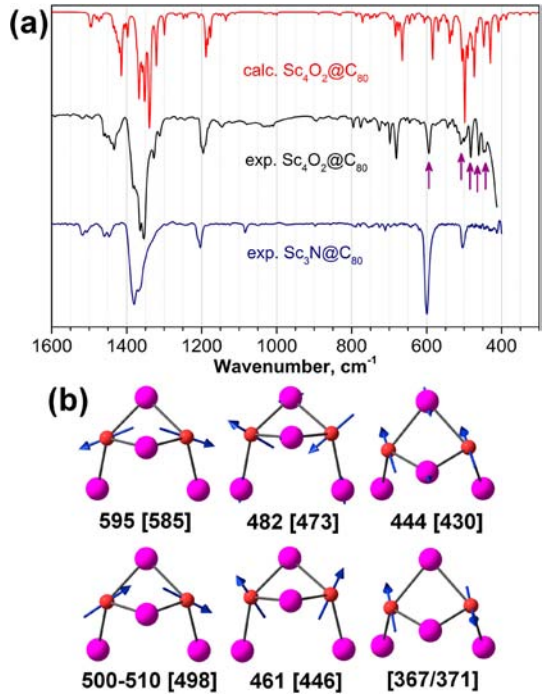


**Figure 3.** (a) IR spectra of $Sc_4O_2@C_{80}$ and $Sc_3N@C_{80}$ compared to the DFT-computed spectrum of $Sc_4O_2@C_{80}$. Cluster-based modes are highlighted by arrows. (b) Vibrational displacements of the modes with a predominant oxygen contribution. The numbers below each structure are experimental and computed (in brackets) vibrational frequencies.

$Sc_4O_2$ cluster imposes a larger distortion of the cage than the $Sc_3N$ cluster.

At 594 $cm^{-1}$, $Sc_3N@C_{80}$ has a strong band corresponding to the 2-fold degenerate antisymmetric M−N stretching mode,[48] which provides important structural information on the nitride cluster and can be described as the in-plane motion of the nitrogen atom (an out-of-plain motion, i.e., a $\gamma(Sc_3N)$ mode, occurs at 236 $cm^{-1}$).[49] In the $Sc_4O_2$ cluster, a large difference in the masses of scandium and oxygen results in an almost complete separation of the O and Sc motions. According to DFT computations, six vibrations corresponding to the displacements of the oxygen atoms are distributed in the range of 400−600 $cm^{-1}$. These modes can be classified into three pairs on the basis of the types of oxygen displacements, and each type has two counterparts with the in-phase and out-of-phase motions of two oxygen atoms.

The highest frequency cluster mode at 594 $cm^{-1}$ is the in-phase motion of oxygen atoms approximately parallel to the O-coordinated $Sc_3$ faces with the largest contributions from $Sc^{II}$−O stretching (Figure 3b) and can be denoted as $\nu(Sc^{II}-O)$. The other five modes partially mixed with the cage vibration fall in the 400−500 $cm^{-1}$ range. Due to the high polarity of the Sc−O bonds, these vibrations also have medium to strong IR intensities, but their assignment to the experimental bands is more ambiguous because of the interference with the absorption of the KBr substrate. The out-of-phase $\nu(Sc^{II}-O)$ mode is red-shifted from its in-phase counterpart by ca. 100 $cm^{-1}$, and according to DFT computations, it is the strongest oxygen-based mode of $Sc_4O_2@C_{80}$. In the experimental spectrum it is mixed with several cage modes and presumably corresponds to the broad band near 500−510 $cm^{-1}$.


dx.doi.org/10.1021/ja306728p | J. Am. Chem. Soc. 2012, 134, 19607−19618

The motion of the oxygen atom perpendicular to the $Sc_3$ faces has a predominant contribution to two bands at 482 and 461 $cm^{-1}$ (theoretical values are 473 and 446 $cm^{-1}$, respectively). Finally, two vibrations with an enhanced contribution of $\nu(Sc^{III}–O)$ stretching are predicted at 430 and 367/371 $cm^{-1}$, and in the experimental spectrum the former corresponds to the absorption at 444 $cm^{-1}$. The large difference between the vibrational frequencies of the $\nu(Sc^{II}–O)$ and $\nu(Sc^{III}–O)$ modes agrees well with much shorter DFT-optimized $Sc^{II}–O$ bonds (1.983 Å) in comparison to $Sc^{III}–O$ bonds (2.027/2.041 Å).

The Raman spectra of $Sc_4O_2@C_{80}$ measured at 78 K with two excitation wavelengths are compared in Figure 4 to the

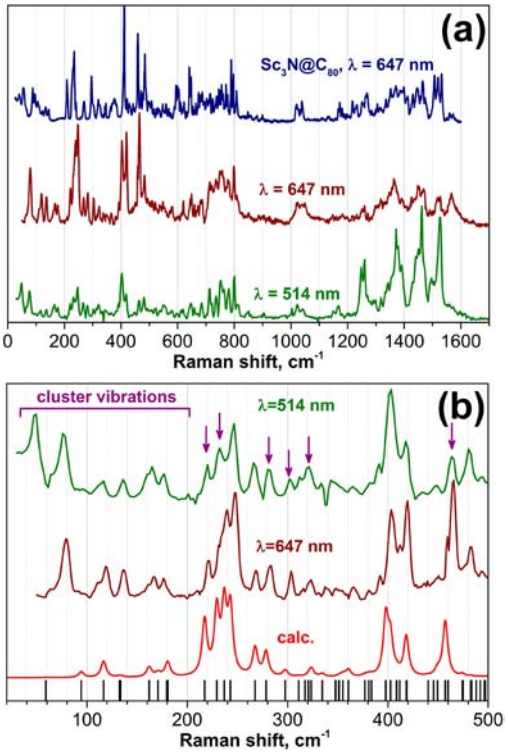


**Figure 4.** (a) Raman spectra of $Sc_4O_2@C_{80}$ excited at 514 and 647 nm and the spectrum of $Sc_3N@C_{80}$ excited at 647 nm. (b) Enlarged low-frequency part of the spectra compared to the results of computations for off-resonance conditions. Black bars denote computed vibrational frequencies. In (b), in the frequency range above 200 $cm^{-1}$, the modes with a large Sc contribution are highlighted by arrows.

spectrum of $Sc_3N@C_{80}$. The spectra show a significant dependence on the excitation wavelength pointing to the preresonant nature of the scattering. In particular, at an excitation wavelength $\lambda_{ex}$ = 514 nm, higher frequency tangential modes (1200–1600 $cm^{-1}$) of the cage are enhanced, whereas in the spectrum excited at $\lambda_{ex}$ = 647 nm the highest intensity is found for the radial cage modes in the 200–500 $cm^{-1}$ range. Although the overall spectral patterns of $Sc_3N@C_{80}$ and $Sc_4O_2@C_{80}$ are similar, the details are distinctly different. These differences can be attributed both to the changes of the cage perturbation by the cluster and to the different electronic structure of $Sc_4O_2@C_{80}$, resulting in different resonant conditions.

In the low-frequency part (below 200 $cm^{-1}$) the spectrum exhibits a group of peaks corresponding to the vibrations of the $Sc_4O_2$ cluster. In terms of the atomic displacements, these modes are essentially Sc motions, and they include both frustrated translational/rotational motions of the cluster and its internal modes. DFT calculations show that the 50–200 $cm^{-1}$ range includes 9 from 12 Sc-related modes, whereas 3 remaining modes are mixed with the cage vibrations and scattered in the 200–350 $cm^{-1}$ range (they are marked by arrows in Figure 4b). In these mixed cluster/cage vibrations the cluster deformations follow those of the carbon cage. The most intense Raman lines of this sort are the two components of the cage squashing mode at 220 and 232 $cm^{-1}$ and the breathing cage mode at 464 $cm^{-1}$ (very strong line in the spectrum excited at 647 nm but weak at the 514 nm excitation; this line corresponds to the IR band at 464 $cm^{-1}$ discussed above). A further description of the displacement patterns of the cluster modes can be found in the Supporting Information.

**Electrochemical Studies.** The results of cyclic and square-wave voltammetry measurements of $Sc_4O_2@C_{80}$ are shown in Figure 5 and summarized in Table 2 (preliminary redox data for

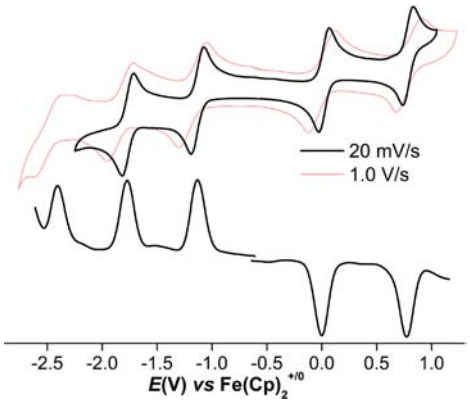


**Figure 5.** Cyclic voltammetry (upper trace, scan rates 20 mV/s and 1 V/s) and square-wave voltammetry of $Sc_4O_2@C_{80}$ in *o*-DCB solution.

$Sc_4O_2@C_{80}$ were reported recently in ref 50). At low voltammetric scan rates (20 mV/s), $Sc_4O_2@C_{80}$ exhibits two reversible oxidation and two reversible reduction steps with an electrochemical (EC) gap of 1.10 V (the DFT-predicted gap reported by Poblet et al. is 0.88 V[32]). A third reduction step can also be observed at higher scan rates or with the use of square-wave voltammetry. The reversible behavior of $Sc_4O_2@C_{80}$ on the cathodic scale is remarkable taking into account the irreversible reductions usually exhibited by clusterfullerenes.[4,51]

The redox potentials of $Sc_4O_2@C_{80}$ are also rather special and require a more detailed analysis. The first oxidation step observed at 0.00 V vs $Fe(Cp)_2^{+/0}$ is substantially more negative than the oxidation potentials of the majority of EMFs with a diamagnetic state of the carbon cage (Table 2). Interestingly, this value is comparable to the oxidation potential of $Sc_2@C_{82}$-$C_{3v}(8)$ (0.05 V).[45] In the latter, the oxidation corresponds to the removal of the electron from the Sc–Sc bonding HOMO, which is similar to the case of $Sc_4O_2@C_{80}$, whose HOMO also has presumably a $Sc^{II}–Sc^{II}$ bonding character. Similar low values of the first oxidation potentials were also reported for nitride clusterfullerenes with a cluster-based oxidation step, including $CeLu_2N@C_{80}$,[36] $TiSc_2N@C_{80}$,[35,52] and $TiY_2N@C_{80}$[39] (Table 2). For comparison, if the first reduction is based on the fullerene (rather than on the endohedral species), the $E_{1/2}(+/0)$ values for the EMFs with the $C_{80}$-$I_h(7)$ carbon


dx.doi.org/10.1021/ja306728p | J. Am. Chem. Soc. 2012, 134, 19607–19618

Table 2. Redox Properties of $Sc_4O_2@C_{80}$ in Comparison to $Sc_2@C_{82}$, $Sc_2O@C_{82}$, and EMFs with a $C_{80}$-$I_h(7)$ Carbon Cage[a]

| | $II_{ox}$ | $I_{ox}$ | $I_{red}$ | $II_{red}$ | $III_{red}$ | EC gap (V) | ref |
|---|---|---|---|---|---|---|---|
| $Sc_4O_2@C_{80}$ | 0.79 | **0.00** | **−1.10** | −1.73 | −2.35 | 1.10 | this work |
| $Sc_2@C_{82}$-$C_{3v}(8)$ | | **0.05** | −1.10 | | | 1.15 | 45 |
| $TiSc_2N@C_{80}$ | | **0.16** | **−0.94** | −1.58 | −2.21 | 1.10 | 35, 52 |
| $TiY_2N@C_{80}$ | | **0.00** | **−1.11** | [−1.79] | | 1.11 | 39 |
| $CeLu_2N@C_{80}$ | | **0.01** | [−1.43] | [−1.92] | | 1.44 | 36 |
| $Sc_4C_2@C_{80}$ | 1.10 | **0.40** | [−1.16] | −1.65 | | 1.56 | 25 |
| $La_2@C_{80}$ | 0.95 | 0.56 | **−0.31** | −1.72 | −2.13 | 0.87 | 37 |
| $Sc_3NC@C_{80}$ | | 0.60 | **−1.05** | −1.68 | | 1.65 | 27 |
| $Sc_3N@C_{80}$ | 1.09 | 0.59 | **−1.26** | −1.62 | −2.37 | 1.85 | 53 |
| $Dy_3N@C_{80}$ | | 0.70 | [−1.37] | [−1.86] | | 2.07 | 54 |
| $Lu_3N@C_{80}$ | [1.11] | [0.64] | [−1.42] | [−1.80] | [−2.26] | 2.08 | 55 |
| $Sc_2O@C_{82}$-$C_s(6)$ | 0.72 | 0.35 | −0.96 | −1.28 | −1.74 | 1.31 | 56 |

[a] $E_{1/2}$ values (V) for reversible redox steps. For electrochemically irreversible processes, peak potentials are listed in square brackets; the first reduction and oxidation potentials are highlighted in bold if they correspond to endohedral redox processes.

cage fall in the range of 0.56−0.70 V ($La_2@C_{80}$, $Sc_3N@C_{80}$, $M_3N@C_{80}$, etc.).

The first reduction potential of $Sc_4O_2@C_{80}$ is found at −1.10 V vs $Fe(Cp)_2^{+/0}$. This value is noticeably more positive than the first reduction potentials of $M_3N@C_{80}$ (here M is Y and lanthanides) with a cage-based reduction near −1.40 V vs $Fe(Cp)_2^{+/0}$ and is close to the reduction potentials of several EMFs with the endohedral reduction step ($TiM_2N@C_{80}$, $Sc_3NC@C_{80}$). Endohedral-based reductions of EMFs with the $C_{80}$-$I_h(7)$ cage are bracketed by $Sc_3N@C_{80}$ (−1.26 V vs $Fe(Cp)_2^{+/0}$, reduction of the $Sc_3N$ cluster) and $La_2@C_{80}$ (−0.31 V, reduction of the $La_2$ cluster). Thus, on the basis of the first reduction potential, it is possible to conclude that $Sc_4O_2@C_{80}$ exhibits an endohedral reduction, which agrees with the results of DFT calculations showing an endohedral localization of the frontier MOs.

$Sc_4O_2@C_{80}$ also exhibits a relatively large difference between the first and second reduction (0.63 V) and oxidation (0.79 V) steps. For the cage-based redox steps, this difference usually spans the range of 0.4−0.5 V (see, e.g., the values for $M_3N@C_{80}$ in Table 2), whereas an enhanced gap between the first and second reduction/oxidation steps points to the metal-based redox processes (e.g., that of the first and second reduction steps of $La_2@C_{80}$ is 1.41 V).

In summary, both the oxidation and reduction of $Sc_4O_2@C_{80}$ are reversible endohedral redox processes. As a result, its electrochemical gap of 1.10 V is almost 2 times smaller than that of $M_3N@C_{80}$, whose oxidation and reduction are localized on the carbon cage. The reversible reduction and oxidation of $Sc_4O_2@C_{80}$ indicate that the cation and anion radicals of this fullerene are stable in *o*-DCB at room temperature and thus can be studied by in situ ESR spectroelectrochemistry.

**ESR Spectroelectrochemistry of $Sc_4O_2@C_{80}$.** The ESR spectrum measured during the oxidation of $Sc_4O_2@C_{80}$ at the first oxidation peak is shown in Figure 6a. The spectrum is nonsymmetric, exhibits a manifold of relatively narrow lines (line width of ca. 3.5 G), and spans a range of more than 2200 G. In spite of the overall complexity, the interpretation of the spectrum is straightforward. The 15-line multiplets of nearly equidistant lines with a hyperfine coupling constant (hfcc) of 18 G at the right wing of the spectrum indicate the presence of two equivalent Sc atoms. The experimental spectrum can then be perfectly reproduced when considering that two other Sc atoms are also equivalent with an hfcc of 150.4 G. Such a giant $a(^{45}Sc)$ value causes the broad range of the spectrum and its

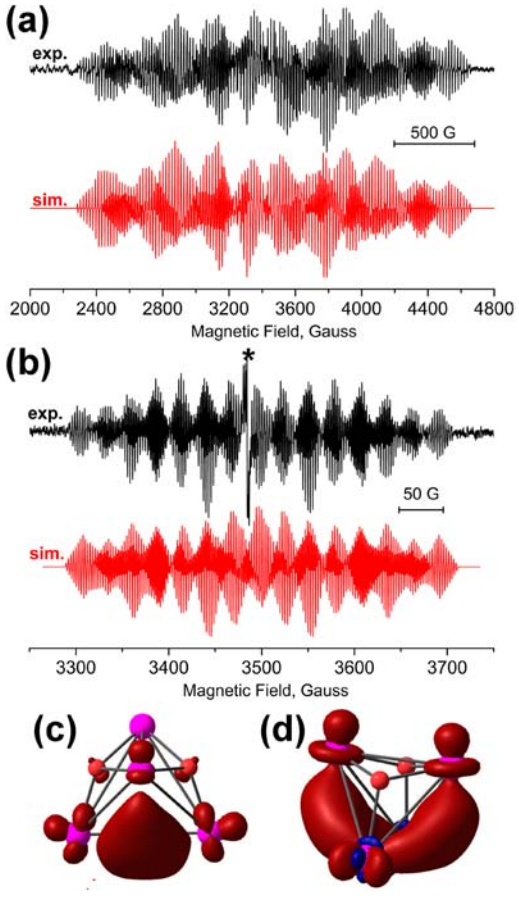


**Figure 6.** (a, b) ESR spectra measured in situ during electrochemical oxidation (a) and reduction (b) of $Sc_4O_2@C_{80}$ at the potentials of the first oxidation/reduction voltammetric peaks. Black lines are experimental spectra, and red lines are simulated spectra. In (b), the asterisk marks an unidentified impurity signal. (c, d) Spin density at the $Sc_4O_2$ cluster in the cation (c) and anion (d).

asymmetry, which is caused by the higher order effects. The *g* factor of the cation radical, $g = 1.9956$, is smaller than the free electron value (2.0023) and points to the localization of the spin density on the metal atoms.

The ESR spectrum of the anion radical spans a field of ca. 400 G and also exhibits a complex hyperfine pattern, which can be simulated by considering two pairs of equivalent Sc atoms with $a(^{45}Sc)$ values of 2.6 and 27.4 G. These values are not


dx.doi.org/10.1021/ja306728p | J. Am. Chem. Soc. 2012, 134, 19607−19618

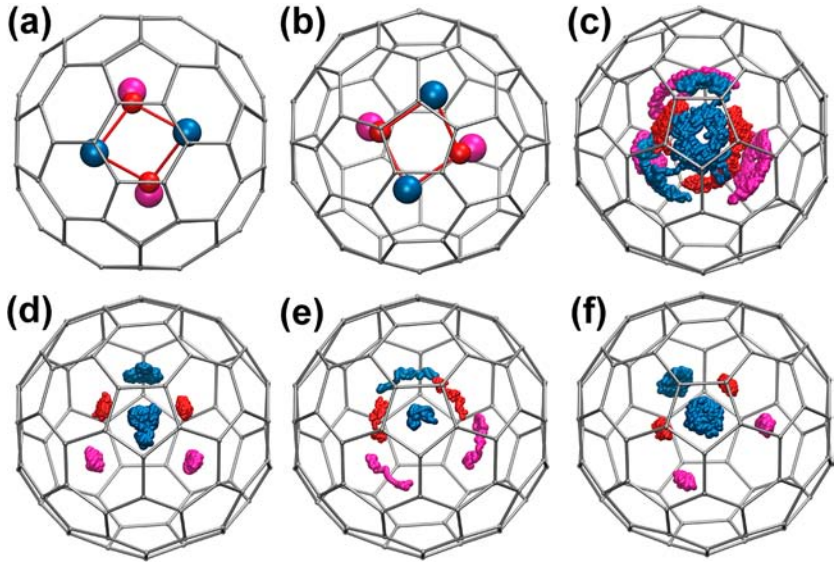


**Figure 7.** (a, b) DFT-optimized conformers **I** (a) and **II** (b) of $Sc_4O_2@C_{80}$. Both structures are shown in such an orientation that the $C_2$ axis of the cluster is perpendicular to the paper. (c–f) Trajectories obtained in the molecular dynamics simulations: (c) cation (the whole trajectory); (d) anion (equilibration and first 12 ps); (e) rearrangement between two conformations (12–13 ps); (f) dwelling near conformation **I** (13–40 ps). See Figure 1 for color codes of the atoms. The structures in (d–f) are shown with the same orientation of the carbon cage (i.e., all visible differences between the structures are due to the rotation of the cluster).

**Table 3. DFT-Computed $a(^{45}Sc)$ Values (G) and $g$ Factors for Selected Conformers of $Sc_4O_2@C_{80}^+$ and $Sc_4O_2@C_{80}^-$**

| | | cation | | | anion | | |
|---|---|---|---|---|---|---|---|
| conf[a,b] | basis set | $a(^{45}Sc^{II})$ | $a(^{45}Sc^{III})$ | $g$ | $a(^{45}Sc^{II})$ | $a(^{45}Sc^{III})$ | $g$ |
| **I**, $C_2$ | def2-TZVP(-g), TZVP[c] | 2 × 120.6 | 2 × 14.4 | 1.9973 | 2 × 10.6 | 2 × 26.4 | 1.9907 |
| | Λ33, Λ2[c] | 2 × 123.7 | 2 × 14.4 | | 2 × 6.4 | 2 × 27.8 | |
| | CP3P, SVP[d] | 2 × 124.5 | 2 × 16.4 | | 2 × 3.2 | 2 × 27.0 | |
| **II**, $C_1$ | def2-TZVP(-g), TZVP[c] | 115.6/135.7 | 11.0/22.7 | 1.9959 | 2.8/14.0 | 11.3/25.0 | 1.9946 |
| | Λ33, Λ2[c] | 118.5/138.6 | 11.2/22.2 | | −1.3/10.6 | 13.4/24.7 | |
| | CP3P, SVP[d] | 119.1/141.9 | 13.7/23.4 | | −3.8/7.3 | 14.9/20.9 | |
| **III**, $C_s$ | def2-TZVP(-g), TZVP[c] | 2 × 98.7 | 2.1/26.5 | 1.9967 | 2 × 67.5 | −8.7/32.6 | 1.9950 |
| | Λ33, Λ2[c] | 2 × 101.1 | 2.5/25.1 | | 2 × 66.0 | −7.5/31.3 | |
| | CP3P, SVP[d] | 2 × 102.4 | 2.9/26.4 | | 2 × 66.2 | −8.9/33.8 | |
| **IV**, $C_1$ | def2-TZVP(-g), TZVP[c] | 105.4/110.3 | 9.5/38.9 | 1.9957 | 20.7/27.0 | 0.5/43.7 | 1.9923 |
| | Λ33, Λ2[c] | 106.7/111.6 | 10.0/38.0 | | 17.8/24.9 | 3.2/43.3 | |
| | CP3P, SVP[d] | 112.8/119.4 | 11.7/35.5 | | 17.1/26.6 | −0.1/40.0 | |
| MD | CP3P, SVP | 122.5/126.5[e] | 18.6/20.4[e] | | 2 × 9.8[f] | 2 × 24.5[f] | |
| exptl | | 2 × 150.4 | 2 × 19.0 | 1.9956 | 2 × 2.6 | 2 × 27.4 | 1.9960 |

[a]Only conformers with similar structures for the cation and anion are listed; see the Supporting Information for further details. [b]Relative energies of the conformers (kJ/mol) computed at the PBE/(TZ2P, SBK) level are 1.7 (**I**), 0.0 (**II**), 8.5 (**III**), and 1.0 (**IV**) for the cation and 0.0 (**I**), 17.2 (**II**), 14.2 (**III**), and 24.4 (**IV**) for the anion. [c]Coordinates are optimized at the PBE/(TZ2P, SBK) level. [d]Coordinates are optimized at the PBE/DZVP level with ECP for Sc. [e]The values are averaged over the period of 0–40 ps. [f]The values are averaged over the period of 15–40 ps and correspond to conformer **I** (see Figure 7a).

sufficiently large to induce significant second-order effects, and the spectrum is almost symmetric. Similar to the case of the cation, the $g$ factor, 1.9960, is noticeably smaller than the free-electron value.

**Assignment of the ESR spectra.** The ESR spectra clearly demonstrate that on the ESR time scale the $Sc_4O_2$ cluster has two pairs of equivalent Sc atoms, which exhibit distinctly different behaviors both in the endohedral redox processes and in their contributions to the spin density. However, the experimental data do not allow a direct assignment of the hfc values to $Sc^{II}$ and $Sc^{III}$. To solve this problem, we have performed extended DFT studies of the structure, dynamics, and $^{45}Sc$ hfc constants in the charged states of $Sc_4O_2@C_{80}$.

Earlier computational studies reported several conformers of $Sc_4O_2@C_{80}$ (by "conformers" here we imply structures with different orientations of the $Sc_4O_2$ cluster with respect to the carbon cage).[32] We used these and several other conformers as a starting point and performed tight optimization of the molecular structures in the anionic, cationic, and neutral forms of the endohedral fullerene at the PBE/(TZ2P, SBK) level. The procedure resulted in four unique conformers for the neutral $Sc_4O_2@C_{80}$ and five unique conformers for both $Sc_4O_2@C_{80}^+$ and $Sc_4O_2@C_{80}^-$ (see Figure 7a,b and the Supporting Information for more details).

*Cation.* For the cation, four conformers are virtually isoenergetic (relative energies are within 2 kJ/mol), whereas the relative energy of the fifth conformer is 8.5 kJ/mol. The


dx.doi.org/10.1021/ja306728p | J. Am. Chem. Soc. 2012, 134, 19607–19618

small energy range of the conformers is an indication of the cluster rotation without any preferable localization site. Table 3 lists the hfc values of the four conformers computed with the Perdew–Burke–Ernzerhof (PBE) functional and different basis sets.

The variation of the predicted $a(^{45}Sc)$ values with the basis sets does not exceed several gauss, and all methods agree that the hfc constants corresponding to $Sc^{II}$ atoms are much larger than those of $Sc^{III}$. At the same time, the values exhibit significant variations depending on the orientation of the cluster with respect to the carbon cage. To get more information on the cluster dynamics and its influence on the $a(^{45}Sc)$ constants, we performed molecular dynamics (MD) simulations at 300 K at the PBE/DZVP level. Figure 7c shows the trajectory of the rotational/vibrational motions of the cluster inside the cage obtained over a period of 40 ps after 15 ps of equilibration. The cluster exhibits large rotational displacements (i.e., rotation is virtually free), which means that not only the relative energies of the conformers but also the barriers to internal rotation are small. In general, Sc atoms prefer to occupy positions near the pentagon/hexagon (5/6) edges, and the rotation of the cluster can be described as a jumping of Sc atoms between different 5/6 edges of the symmetric $C_{80}$-$I_h$ cage. A similar dynamic behavior of metal atoms was described by earlier MD studies of other clusterfullerenes.[35,57−59]

At the next step, we computed $a(^{45}Sc)$ values, sampling each 5 fs of the trajectory (totally 8000 single-point calculations were performed; see refs 59−61 for the use of MD simulation for computations of ESR parameters). The hfc constants were obtained at the PBE level with SVP and TZVP basis sets for C and O, respectively, and a specially tailored CP3P basis for Sc, which has an extended core part and is known to provide good agreement but still remain computationally efficient. For comparison, Table 3 also lists the values computed with this combination of basis sets for the conformers optimized at the PBE/DZVP level (i.e., the level of theory used in MD simulations). As can be seen, the values are not substantially different from those computed using the extended Λ33 basis set for Sc atoms.

Figure 8 shows instant $a(^{45}Sc)$ values at each moment of the MD propagation. The values averaged over the trajectory are also plotted as a function of the propagation time. In spite of the very large variations of the instant hfc constants (ca. 80−160 G for $Sc^{II}$ and ca. 0−50 G for $Sc^{III}$), it takes only a few picoseconds to converge the averaged values (after the first 5 ps, variation of the values does not exceed 5 G). The final $a(^{45}Sc)$ values obtained with dynamic effects taken into account are 124.5 G for $Sc^{II}$ and 19.5 G for $Sc^{III}$, in good agreement with the experimental data and the results of the static DFT calculations.

*Anion.* Computational studies of the $Sc_4O_2@C_{80}^-$ anion revealed that its internal rotation has a more complex mechanism than that in the cation. DFT predicts enhanced stability of conformer **I**, whose relative energy is at least 14 kJ/mol below that of the next most stable structure (conformer **III**). The $a(^{45}Sc)$ values in the anion are much more dependent on the orientation of the cluster, as can be seen in Table 3. For instance, whereas the values for conformer **I** indicate that $a(^{45}Sc^{II})$ is smaller than $a(^{45}Sc^{III})$, an opposite conclusion may be drawn on the basis of the values predicted for conformer **III**. Hence, it is crucial to take possible dynamic effects into account for a reliable prediction of the hfc constants.

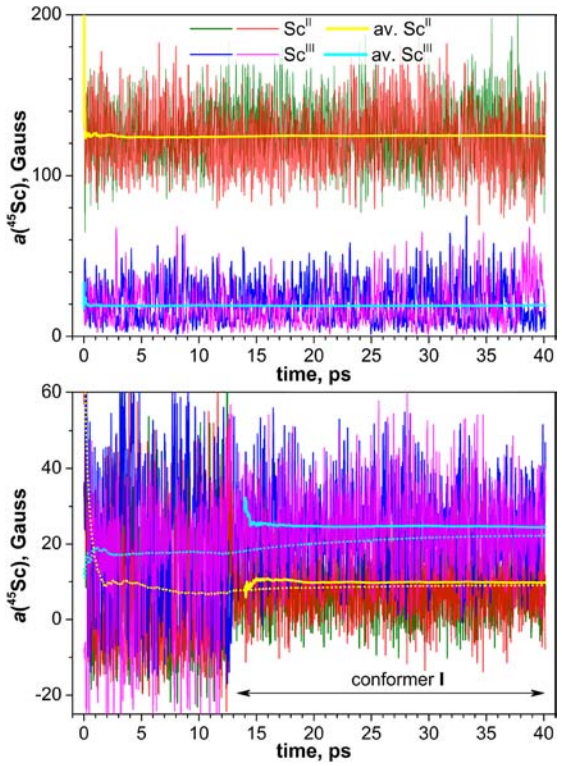


**Figure 8.** Instant and time-averaged $a(^{45}Sc)$ values in the cation (a) and anion (b) of $Sc_4O_2@C_{80}$ sampled along the MD trajectories. Green and red lines are instant hfc constants of $Sc^{II}$, blue and magenta lines are instant hfc constants of $Sc^{III}$, and yellow and cyan lines are averaged values for $Sc^{II}$ and $Sc^{III}$, respectively. In (b), dotted lines show averaging over the whole trajectory, whereas solid lines denote the averaging over the period of 13−40 ps.

MD simulations performed similarly to those already described for the cation proved that the anion has a more complex rotational behavior. The simulations were started from conformer **II**, and during the 15 ps of equilibration and the first 12 ps of the production run, the cluster reoriented fast between conformers **II** and **IV** as can be seen in Figure 7d (besides, conformer **II** is somewhat distorted from $C_s$ symmetry and can easily rearrange into its mirror image). After 13 ps, the cluster reoriented to conformer **I** and remained near this position for the next 27 ps until the end of the MD run, showing only vibrational displacements (see Figure 7e,f for the trajectories). These data show that the rotation of the cluster in the anion is more hindered than in the cation (for the latter, dwelling times in each conformation do not exceed a few picoseconds).

To reconstruct a section of the potential energy surface (PES) describing rotation of the $Sc_4O_2$ cluster, we have optimized transition states on the pathways between different conformers. Then intrinsic reaction coordinate (IRC) calculations were performed to follow the descent of the system to the valleys of the energy minima. Figure 9 plots a fragment of the PES cut along the IRC describing a series of rotational rearrangements of the cluster on the path **I** → **III** → **II** → **V** → **IV**. Conformers **III** and **V** are only shallow pits on the PES with very small barriers (less than 2−3 kJ/mol; see the Supporting Information for more details). The minima corresponding to conformers **II** and **IV** are somewhat deeper, but the escape barriers are still within the range of several kilojoules per mole. In contrast, conformer **I** is much more stable, and the barrier to escape exceeds 26 kJ/mol. Computations of the $a(^{45}Sc)$ values


dx.doi.org/10.1021/ja306728p | J. Am. Chem. Soc. 2012, 134, 19607−19618

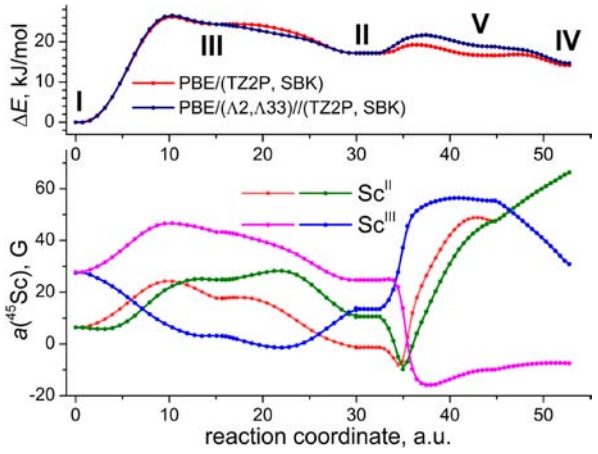


**Figure 9.** Energy profile (upper curve) and $a(^{45}Sc)$ values in the $Sc_4O_2@C_{80}^-$ anion obtained along the IRC path **I** → **III** → **II** → **V** → **IV**. IRC computations were performed at the PBE/(TZ2P, SBK) level, and hfc constants were computed at the PBE/(Λ2, Λ33) level.

along the IRC path (Figure 9) show a very high sensitivity of the hfc constants to the small variations of the position of the cluster; such a high sensitivity of $a(^{45}Sc)$ values to the cluster orientation resembles similar effects found for the $Sc_3N$ cluster in $Sc_3N@C_{80}^-$ and $Sc_3N@C_{80}(CF_3)_2$.[59,62]

On the basis of the MD and IRC calculations, we conclude that the rotational PES in $Sc_4O_2@C_{80}^-$ is rather shallow except for the relatively deep valleys corresponding to conformer **I**. Hence, the cluster can rotate in the anion easily unless it adopts conformation **I**, where it remains trapped with a low probability of escape (and hence long dwelling time). As a result, the rotation of the cluster can be described as jumplike rearrangements between different conformations with the high statistical weight of conformer **I**.

Figure 8b plots instant and time-averaged hfc constants of the $Sc_4O_2@C_{80}^-$ anion computed along the MD trajectory. Two regions of the plot can be distinguished in accordance with the trajectories depicted in Figure 7. During the first 12 ps the $a(^{45}Sc)$ values vary in the ranges of −10 to +50 and −15 to +40 G for $Sc^{III}$ and $Sc^{II}$, respectively. The average values slowly converge to $a(^{45}Sc^{III})$ = 17 G and $a(^{45}Sc^{III})$ = 6 G. When the cluster adopts conformation **I** and starts to librate near this energy minimum, the range in which instant hfc constants oscillate decreases almost twice to 10−40 G for $Sc^{III}$ and −5 to +25 G for $Sc^{II}$. Vibrationally averaged $a(^{45}Sc)$ values for conformer **I** are 24.5 G for $Sc^{III}$ and 9.8 G for $Sc^{II}$. These values are somewhat different from those obtained for conformer **I** in static DFT calculations, but both approaches agree that the experimental hfc constant of 27.4 G should be assigned to $Sc^{III}$, whereas the hfc constant of 2.6 G is due to $Sc^{II}$. Note that a very good match to the experimental hfc constants provided by static calculation at the PBE/(CP3P, SVP)//DZVP level should be attributed to the fortuitous cancellation of errors since both extension of the basis sets and dynamical averaging worsen the agreement with the experiment. At the same time, this result shows that preliminary computationally efficient estimations of the $a(^{45}Sc)$ values in EMFs can be done by this approach.

**Discussion of hfc Constants.** As the assignment of hfc values is clarified by extended static and dynamical DFT calculations, we can now analyze the hfc constant of the cation and anion and discuss the factors affecting their values. Table 4 compares the $a(^{45}Sc)$ values and *g* factors in the cation and anion of $Sc_4O_2@C_{80}$ to those of other paramagnetic Sc-EMFs. Before this work, the largest $a(^{45}Sc)$ value of 55.4−55.6 G was reported for the anion radical $Sc_3N@C_{80}^-$.[38,53,63] In this anion, the spin density is uniformly distributed among three Sc atoms and has the main contribution from $3d_{z^2}$ orbitals of Sc. In the anions of the trifluoromethylated $Sc_3N@C_{80}$ the hfc constants are reduced to less than 20 G (except for the trianion $Sc_3N@C_{80}(CF_3)_2^{3-}$, in which one $a(^{45}Sc)$ constant is 49 G).[63,64] In all other paramagnetic Sc-EMFs, including mono-EMFs,[65−67] $Sc_3C_2@C_{80}$ and its derivatives,[22,65,68−71] and the charged states of $Sc_3N@C_{68}$,[72,73] the $^{45}Sc$ hfc constants do not exceed 10 G, which is not surprising taking into account the low contributions of Sc atoms to the spin density in these radicals.

**Table 4. Isotropic $a(^{45}Sc)$ Constants (G) and *g* Factors of Sc-Based EMF Radicals and Selected Sc-Centered Radicals[a]**

| | $a(^{45}Sc)$, G | *g* factor | conditions | ref |
|---|---|---|---|---|
| $Sc_4O_2@C_{80}^+$ | 2 × 18.0, 2 × 150.4 | 1.9956 | RT/*o*-DCB | [c] |
| $Sc_4O_2@C_{80}^-$ | 2 × 2.6, 2 × 27.4 | 1.9960 | RT/*o*-DCB | [c] |
| $Sc@C_{82}$ | 3.82 | 1.9998 | RT/toluene | 65 |
| $Sc_3C_2@C_{80}$ | 3 × 6.22 | 1.9985 | RT/toluene | 65 |
| $Sc_3N@C_{68}^+$ | 3 × 1.28 | 2.0010 | RT/*o*-DCB | 72 |
| $Sc_3N@C_{68}^-$ | 3 × 1.75 | 2.0032 | RT/*o*-DCB | 73 |
| $Sc_3N@C_{80}^-$ | 3 × 55.6 | 1.9984 | RT/THF | 38 |
| $ScX_2$[b] | 70.3−78.5 | 1.970−1.995 | 14 K/Ar | 74 |
| ScO | 718 | 1.998 | 4 K/Ar | 75, 76 |
| ScS | 664 | 1.994 | 4 K/Ar | 75 |
| $Sc_2$ ($^5\Sigma_u^-$) | 90 | 2.00 | 4 K/Ne | 80 |
| $Sc_2^+$ ($^4\Sigma_g^-$) | 9.5 | 1.973 | 4 K/Ne | 81 |

[a] See the Supporting Information for the extended version of the table. [b] X = F, Cl, Br, CN. [c] This work.

Following the endohedral localization of the HOMO and LUMO in the neutral $Sc_4O_2@C_{80}$ on the cluster (Figure 1), the spin densities in the cation and anion are also presumably localized on the Sc atoms (Figure 6), which obviously results in enhanced $a(^{45}Sc)$ values. However, the large difference between the hfc constants of the cation and the anion and unusually large $a(^{45}Sc^{II})$ value in the cation require further clarification.

Isotropic hyperfine coupling constants in ESR are proportional to the spin density at the position of the nuclei. Since atomic orbitals with angular momentum $l \geq 1$ (p, d, f, ...) have nodes at the nuclei, their contribution to the spin density has only a limited effect on the isotropic hfc constants via polarization of the core and valence s orbitals. The size of the isotropic hyperfine coupling constants is thus mainly determined by the *n*s orbital contributions to the spin density: the large contributions of *n*s orbitals to the singly occupied molecular orbital (SOMO) (and therefore the spin density) lead to a large hfc constant. Table 5 lists the angular momentum resolved Mulliken spin populations of $Sc^{II}$ and $Sc^{III}$ atoms in $Sc_4O_2@C_{80}^+$ and $Sc_4O_2@C_{80}^-$ (the values are computed for the $C_2$-symmetric conformer **I**). In the cation, the total spin populations of $Sc^{II}$ atoms are 49%, with s contributions of 14%. The spin populations of $Sc^{III}$ atoms are only 4%, with a small and negative s contribution. In the anion, the total spin populations of $Sc^{III}$ are increased to 37%, 7% of which are contributed by s orbitals. The spin populations of $Sc^{II}$ are reduced to 21% and have negligible s contributions. These values are in qualitative agreement with the hfc values. In particular, the large $a(^{45}Sc^{II})$ value in the cation correlates with an enhanced contribution of the $Sc^{II}$ 4s orbital to the spin


dx.doi.org/10.1021/ja306728p | J. Am. Chem. Soc. 2012, 134, 19607−19618

**Table 5. Total and Angular Momentum Resolved Mulliken Spin Populations (%) in Selected Sc-Based Radicals and DFT-Predicted hfc Constants (G)[a]**

| molecule | total | s | p | d | hfc |
|---|---|---|---|---|---|
| $Sc_4O_2@C_{80}^+$, $Sc^{II}$ | 48.7 | 13.5 | 15.2 | 19.4 | 120.6 |
| $Sc_4O_2@C_{80}^+$, $Sc^{III}$ | 4.1 | 4.6 | −4.3 | 3.2 | 14.4 |
| $Sc_4O_2@C_{80}^-$, $Sc^{II}$ | 21.1 | −0.7 | −0.8 | 23.5 | 10.6 |
| $Sc_4O_2@C_{80}^-$, $Sc^{III}$ | 37.2 | 6.9 | 11.8 | 17.4 | 26.4 |
| $Sc_3N@C_{80}^-$ | 26.2 | 6.2 | 3.0 | 17.4 | 24.7 |
| | | | | | |
| $Sc^{2+}$ | 100.0 | 0.0 | 0.0 | 100.0 | −32.3 |
| $Sc(CN)_2$ | 102.7 | 30.5 | 5.3 | 66.9 | 251.5 |
| ScO | 105.0 | 83.3 | 10.1 | 12.2 | 630.2 |
| $Sc_2$ ($^5\Sigma_u^-$) | 200.0 | 40.2 | 18.1 | 141.2 | 78.2 |
| $Sc_2^+$ ($^4\Sigma_g^-$) | 150.0 | −1.2 | 9.5 | 141.0 | −5.2 |

[a]All structures were optimized at the PBE/(TZ2P, SBK) level, and spin populations and hfc constants were computed at the PBE/(def2-TZVP(-g), TZVP) level.

density. However, hfc constants are not directly proportional to the s contribution, and the correlation has a more complex nature.

Note that, in the $Sc_3N@C_{80}^-$ anion radical with the second largest $a(^{45}Sc)$ constant among all Sc-EMFs, the s contributions are 6% (versus a total value of 26% for each Sc atom), whereas the d atomic orbitals (AOs) contribute 17%. These values are similar to those found for $Sc^{III}$ in the $Sc_4O_2@C_{80}^-$ radical anion, and DFT predicts almost identical hfc constants. A significant underestimation of the experimental $a(^{45}Sc)$ value in $Sc_3N@C_{80}^-$ by theory was recently explained by dynamical effects.[59]

To illustrate the interplay between d and s contributions to the spin density and its influence on the hfc constants, we also analyzed small Sc-based radicals. $Sc^{2+}$ is essentially a $d^1$ system; as such, it has a zero s contribution to the SOMO. Polarization of the core s orbitals by the valence $3d^1$ SOMO results in a negative $a(^{45}Sc)$ value (Table 5). $ScX_2$ species (X = F, Cl, Br, CN) are similar to $Sc^{2+}$ in that they also have a predominant $3d^1$ component, but the non-negligible s component in the SOMO leads to hfc constants of 70−80 G[74] (Table 4; note that DFT severely overestimates the s component in $Sc(CN)_2$ and consequently the hfc constant; estimation based on the experimental anisotropy parameters yields an s contribution of 7−8%). An opposite situation is found in ScO (and ScS).[75,76] In this radical, scandium forms a triple bond to the oxygen,[77] and its SOMO is largely of Sc $4s^1$ character (the s contribution to the spin population of Sc is 83%). Such an electronic structure results in a very large $a(^{45}Sc)$ constant of 718 G[75,76] (Table 4; theory gives 630 G). The last example specifically emphasizes that an enhanced 4s contribution to the SOMO is crucial for large $a(^{45}Sc)$ values.

The reason for the enhanced s contribution in the $Sc_4O_2@C_{80}^+$ cation can be explained by the analysis of the electronic structure of a $Sc_2$ dimer. The ground state of $Sc_2$ is a quintet, $(4s)\sigma_g^2(3d)\pi_u^2(3d)\sigma_g^1(4s)\sigma_u^1$.[78,79] The highest energy $\sigma_u^1$ SOMO is largely built from 4s AOs, and hence, the s contribution to the spin density in $Sc_2$ is considerable (40% for each Sc atom) and the $a(^{45}Sc)$ value is 90 G.[80] The single-electron oxidation of $Sc_2$ depopulates the $(4s)\sigma_u^1$ SOMO, resulting in an ionic $Sc_2^+$ dimer with negligible s contributions to the total spin population and an $a(^{45}Sc)$ value reduced to 9.5 G.[81] The removal of electrons from the four singly occupied MOs of $Sc_2$ ($\pi_u^2$, $\sigma_g^1$, and $\sigma_u^1$) results in a $Sc_2^{4+}$ dimer whose single Sc−Sc bonding MO resembles a $(4s)\sigma_g^2$ orbital of the $Sc_2$ dimer. In a similar fashion, the HOMO of $Sc_4O_2@C_{80}$, which is essentially a $Sc^{II}$−$Sc^{II}$ bonding MO, also inherits a large 4s component from the $(4s)\sigma_g^2$ MO of the $Sc_2$ dimer. The oxidation of $Sc_4O_2@C_{80}$ removes an electron from the $Sc^{II}$−$Sc^{II}$ bonding MO, yielding the SOMO with an enhanced 4s contribution.

The relation between the Sc−Sc bonding HOMO and large hfc constant of the $Sc_4O_2@C_{80}^+$ cation is an example of the more general situation typical for metal−metal bonding MOs in dimetallofullerenes.[7] Such MOs are usually HOMOs (e.g., in $Sc_2@C_{82}$,[45] $Y_2@C_{82}$,[33] or $Lu_2@C_{76}$[82]) or LUMOs (e.g., in all dilanthanofullerenes) and also resemble $(ns)\sigma_g^2$ MOs of the corresponding metal dimers.[7] As a result, large metal-based hfc constants can be expected in the corresponding radicals. For instance, the LUMO of $La_2@C_{80}$ is a La−La bonding MO, and the $a_{iso}(^{139}La)$ value in the $La_2@C_{80}^-$ anion radical is as large as 386 G.[83] Likewise, the SOMO of $Y_2@C_{79}N$ has Y−Y bonding character, resulting in a large $a(^{89}Y)$ value of 81.2 G.[84] In $Sc_2@C_{82}$, the HOMO is a Sc−Sc bonding MO, and thus, it can be anticipated that the $a(^{45}Sc)$ value in the $Sc_2@C_{82}^+$ cation can be even larger than in $Sc_4O_2@C_{80}^+$. These data show that large metal-based coupling constants in paramagnetic EMFs can serve as indicators of the metal−metal bonds, which makes ESR spectroscopy an important *experimental* tool in the studies of metal−metal bonding interactions in EMFs.

## CONCLUSIONS

In this work we studied electrochemical properties of $Sc_4O_2@C_{80}$ and followed the spin density distribution in the electrochemically generated cation and anion radicals by means of in situ ESR spectroelectrochemistry. The compound with two reversible reduction and oxidation steps and a relatively small electrochemical gap of 1.10 V exhibits an unprecedented endohedral redox behavior for both reduction and oxidation steps. The endohedral electron transfers form ion radicals with $Sc_4O_2$-localized spin density, resulting thus in the rich $^{45}Sc$ hyperfine structure in the ESR spectra. The experimental determination of the $a(^{45}Sc)$ values of two types of Sc atoms in the $Sc_4O_2$ cluster was accomplished with the help of extended DFT and molecular dynamics simulations. Sc atoms in the divalent state in the neutral $Sc_4O_2@C_{80}$ and in the radical cation exhibited an especially large coupling constant, 150.4 G, which is the record high $a(^{45}Sc)$ value for Sc-based endohedral metallofullerenes. Such a high value was explained by the nature of the HOMO in $Sc_4O_2@C_{80}$, which is presumably a Sc−Sc bonding MO and hence has large contributions from 4s atomic orbitals of $Sc^{II}$ atoms. We claim that ESR spectroelectrochemistry is an invaluable experimental tool in the studies of metal−metal bonding in EMFs and in endohedral electrochemistry.

## EXPERIMENTAL AND COMPUTATIONAL DETAILS

Soot containing $Sc_4O_2@C_{80}$ was prepared using the CAPTEAR method.[85] The oxidizing environment in the reactor uses $O_2$ from air and $NO_x$ vapor via the decomposition of copper nitrate hydrate. Scandium soot extracts containing $Sc_4O_2@C_{80}$,[28] $Sc_4O_3@C_{80}$,[29] and $Sc_2O@C_{82}$[86] and details of the arc synthesis have been described previously.[87] As the extract still contains a majority of empty-cage fullerenes, an initial precleanup stage with a Lewis acid, $AlCl_3$, was performed to remove these abundant contaminants (e.g., $C_{60}$, $C_{70}$, $C_{76}$, $C_{78}$, and $C_{84}$).[88] After a selective complexation−decomplexation step, a metallofullerene sample enriched in $Sc_4O_2@C_{80}$ was obtained. A multistage high-performance liquid chromatography (HPLC) procedure was utilized to further isolate and purify $Sc_4O_2@C_{80}$; see the


dx.doi.org/10.1021/ja306728p | J. Am. Chem. Soc. 2012, 134, 19607−19618

Supporting Information for HPLC details and the mass spectrum of the purified compound.

**Spectroscopic and Electrochemical Studies.** The 125 MHz $^{13}C$ NMR and 121.5 MHz $^{45}Sc$ spectra were measured at room temperature in carbon disulfide and *o*-DCB solutions with $d_6$-acetone as a lock on an Avance 500 spectrometer (Bruker, Germany) using the multiprobe head PH 1152Z.

For IR and Raman measurements, the sample was drop-coated onto single-crystal KBr disks. The residual toluene was removed by heating the polycrystalline films in a vacuum at 200 °C for 3 h. The FTIR spectra were recorded at room temperature in transmission mode by a Vertex 80v spectrometer (Bruker, Germany) with a resolution of 2 $cm^{-1}$. Raman spectra were recorded at 78 K on a T 64000 triple spectrometer (Jobin Yvon, France) with visible laser radiation at 647 and 514 nm (Innova 300 series, Coherent, Santa Clara, CA).

**Electrochemical and Spectroelectrochemical Measurements.** Cyclic voltammetry measurements were carried out in a glovebox (water and oxygen contents below 1 ppm) in a one-compartment electrochemical cell. The electrolyte solution was 0.1 M $N(n\text{-}Bu)_4BF_4$ in dichlorobenzene. Platinum wires and a silver wire served as the working, counter, and pseudoreference electrodes, respectively. The potentials were measured against an $Fe(Cp)_2^{+/0}$ couple; i.e., $Fe(Cp)_2$ was added as the internal standard at the end of the measurements. Potentials were controlled by a PAR 273 potentiostat/galvanostat.

The cell for ESR spectroelectrochemistry using a laminated Pt-mesh working electrode, a Pt-wire counter electrode, and a silver wire quasi-reference electrode has been described in detail previously.[89,90] The cell was filled with a $Sc_4O_2@C_{80}$ solution in a glovebox, then tightly closed, and transferred into the cavity of an X-band EPR spectrometer (EMX Bruker, Germany), where the spectroelectrochemical measurements were done. Potentials were controlled by a HEKA potentiostat/galvanostat system (HEKA Elektronik, Lambrecht/Pfalz, Germany). ESR spectra were simulated using the EasySpin suite.[91]

**Quantum-Chemical Computations.** Optimization of the molecular structures was performed using the PBE exchange-correlation functional[92] and TZ2P-quality basis set (full-electron {6,3,2}/(11s,6p,2d) for C, N, and F atoms and SBK-type effective core potential for Sc atoms with a {5,5,4}/(9s,9p,8d) valence part) implemented in the PRIRODA package.[93,94] This basis set is abbreviated here as (TZ2P, SBK). The code employed expansion of the electron density in an auxiliary basis set to accelerate evaluation of the Coulomb and exchange-correlation terms.[93] Anion and cation radicals were studied in their doublet state.

In computations of hfc constants with the PRIRODA code we used the PBE functional and Λ2 basis set {4,3,2,1}/(12s,8p,4d,2f) for carbon atoms and extended Λ33 basis for O, {8,7,5,3,1}/(14s,10p,7d,5f,3g), and Sc, {10s,9p,7d,5f,3g,1h}/{27s,22p,16d,10f,8g,4h).[95] Computations of hfc constants with the ORCA package[96,97] were performed with two combinations of basis sets. One employed the TZVP {5,3,1}/(11s,6p,1d) basis set[98] for carbon atoms and def2-TZVP basis sets[99] for O, {5,3,2}/(11s,6p,2d), and Sc, {6,5,4,2}/(17s12p7d2f) (f and g polarization functions were removed from the original def2-TZVP basis for O and Sc, respectively); these basis sets were also used in the computations of *g* factors by the mean-field method implemented in ORCA. For computations of hfc constants along MD trajectories, we used the SVP basis for carbon, TZVP basis for oxygen, and core-property CP3P basis[100] for Sc, {17,6,3}/(17s,10p,5d) (see ref 101 for benchmarking computations of hfc constants in transition-metal compounds using the CP3P basis set). NMR chemical shifts were computed at the GIAO-PBE/Λ2 level using the Priroda code.

Born–Oppenheimer molecular dynamics calculations were performed in the CP2K code[102,103] and employed the velocity Verlet algorithm with a time step of 0.5 fs and a Nosé–Hoover thermostat set at 300 K. Calculations were performed with the PBE functional and employed the Gaussian and plane wave (GPW) scheme with Goedecker–Teter–Hutter pseudopotentials and the DZVP basis set.[102,104,105]

Visualization of the structures, trajectories, and isosurfaces was done with Chemcraft[106] and VMD.[107]

## ■ ASSOCIATED CONTENT

### Supporting Information

Details of the HPLC separation, Cartesian coordinates, DFT-calculated $^{45}Sc$ chemical shifts, vibrational displacements, and isotropic $a(^{45}Sc)$ constants and *g* factors of Sc-based radicals. This material is available free of charge via the Internet at http://pubs.acs.org.

## ■ AUTHOR INFORMATION


### Corresponding Author

a.popov@ifw-dresden.de; stevenss@ipfw.edu; echegoyen@utep.edu; l.dunsch@ifw-dresden.de

### Present Addresses

[#]College of Chemistry, Chemical Engineering and Materials Science, Soochow University, Suzhou, Jiangsu 215123, China.
[▽]Universidad Santo Tomás, 680006 Bucaramanga, Colombia.


### Notes

The authors declare no competing financial interest.

## ■ ACKNOWLEDGMENTS


We are thankful to Sandra Schiemenz (IFW Dresden) for her help with the NMR and vibrational spectroscopic measurements and to Ulrike Nitzsche for assistance with local computational resources in IFW Dresden. The Research Computing Center of Moscow State University is acknowledged for time on the supercomputer SKIF-Chebyshev. Time-demanding molecular dynamics simulations were performed on the supercomputer JUROPA at the Jülich Supercomputing Center with a grant from FZ-Jülich. A.A.P. is thankful to DFG (Project PO 1602/1-1) for financial support. S.S. thanks the National Science Foundation, Grant CHE-1151668. L.E., N.C., and J.P. thank the National Science Foundation, Grants CHE-1110967 and CHE-1124075, for generous financial support as well as the Robert A. Welch Foundation for an endowed chair to L.E., Grant AH-0033.


## ■ REFERENCES


(1) Shinohara, H. *Rep. Prog. Phys.* **2000**, *63* (6), 843–892.
(2) Akasaka, T.; Nagase, S. *Endofullerenes: A New Family of Carbon Clusters*; Kluwer: Dordrecht, The Netherlands, 2002.
(3) Dunsch, L.; Yang, S. *Small* **2007**, *3* (8), 1298–1320.
(4) Chaur, M. N.; Melin, F.; Ortiz, A. L.; Echegoyen, L. *Angew. Chem., Int. Ed.* **2009**, *48*, 7514–7538.
(5) Rodriguez-Fortea, A.; Balch, A. L.; Poblet, J. M. *Chem. Soc. Rev.* **2012**, *40*, 3551–3563.
(6) Yang, S.; Liu, F.; Chen, C.; Jiao, M.; Wei, T. *Chem. Commun.* **2011**, *47* (43), 11822–11839.
(7) Popov, A. A.; Avdoshenko, S. M.; Pendás, A. M.; Dunsch, L. *Chem. Commun.* **2012**, *48*, 8031–8050.
(8) Stevenson, S.; Rice, G.; Glass, T.; Harich, K.; Cromer, F.; Jordan, M. R.; Craft, J.; Hadju, E.; Bible, R.; Olmstead, M. M.; Maitra, K.; Fisher, A. J.; Balch, A. L.; Dorn, H. C. *Nature* **1999**, *401* (6748), 55–57.
(9) Stevenson, S.; Fowler, P. W.; Heine, T.; Duchamp, J. C.; Rice, G.; Glass, T.; Harich, K.; Hajdu, E.; Bible, R.; Dorn, H. C. *Nature* **2000**, *408* (6811), 427–428.
(10) Dunsch, L.; Krause, M.; Noack, J.; Georgi, P. *J. Phys. Chem. Solids* **2004**, *65* (2–3), 309–315.
(11) Krause, M.; Wong, J.; Dunsch, L. *Chem.—Eur. J.* **2005**, *11* (2), 706–711.

(12) Yang, S. F.; Dunsch, L. *J. Phys. Chem. B* **2005**, *109* (25), 12320−12328.
(13) Chaur, M. N.; Melin, F.; Elliott, B.; Athans, A. J.; Walker, K.; Holloway, B. C.; Echegoyen, L. *J. Am. Chem. Soc.* **2007**, *129* (47), 14826−14829.
(14) Melin, F.; Chaur, M. N.; Engmann, S.; Elliott, B.; Kumbhar, A.; Athans, A. J.; Echegoyen, L. *Angew. Chem., Int. Ed.* **2007**, *46* (47), 9032−9035.
(15) Chaur, M. N.; Melin, F.; Ashby, J.; Kumbhar, A.; Rao, A. M.; Echegoyen, L. *Chem.—Eur. J.* **2008**, *14* (27), 8213−8219.
(16) Olmstead, M. M.; Balch, A. L.; Pinzón, J. R.; Echegoyen, L.; Gibson, H. W.; Dorn, H. C. New Endohedral Metallofullerenes: Trimetallic Nitride Endohedral Fullerenes. In *Chemistry of Nanocarbons*; Akasaka, T., Wudl, F., Nagase, S., Eds.; John Wiley & Sons, Ltd.: Chichester, U.K., 2010; pp 239−259.
(17) Zuo, T. M.; Beavers, C. M.; Duchamp, J. C.; Campbell, A.; Dorn, H. C.; Olmstead, M. M.; Balch, A. L. *J. Am. Chem. Soc.* **2007**, *129* (7), 2035−2043.
(18) Krause, M.; Ziegs, F.; Popov, A. A.; Dunsch, L. *ChemPhysChem* **2007**, *8* (4), 537−540.
(19) Wang, C. R.; Kai, T.; Tomiyama, T.; Yoshida, T.; Kobayashi, Y.; Nishibori, E.; Takata, M.; Sakata, M.; Shinohara, H. *Angew. Chem., Int. Ed.* **2001**, *40* (2), 397−399.
(20) Shi, Z. Q.; Wu, X.; Wang, C. R.; Lu, X.; Shinohara, H. *Angew. Chem., Int. Ed.* **2006**, *45* (13), 2107−2111.
(21) Iiduka, Y.; Wakahara, T.; Nakajima, K.; Tsuchiya, T.; Nakahodo, T.; Maeda, Y.; Akasaka, T.; Mizorogi, N.; Nagase, S. *Chem. Commun.* **2006**, *19*, 2057−2059.
(22) Iiduka, Y.; Wakahara, T.; Nakahodo, T.; Tsuchiya, T.; Sakuraba, A.; Maeda, Y.; Akasaka, T.; Yoza, K.; Horn, E.; Kato, T.; Liu, M. T. H.; Mizorogi, N.; Kobayashi, K.; Nagase, S. *J. Am. Chem. Soc.* **2005**, *127* (36), 12500−12501.
(23) Yang, H.; Lu, C.; Liu, Z.; Jin, H.; Che, Y.; Olmstead, M. M.; Balch, A. L. *J. Am. Chem. Soc.* **2008**, *130* (51), 17296−17300.
(24) Inoue, T.; Tomiyama, T.; Sugai, T.; Okazaki, T.; Suematsu, T.; Fujii, N.; Utsumi, H.; Nojima, K.; Shinohara, H. *J. Phys. Chem. B* **2004**, *108* (23), 7573−7579.
(25) Wang, T.-S.; Chen, N.; Xiang, J.-F.; Li, B.; Wu, J.-Y.; Xu, W.; Jiang, L.; Tan, K.; Shu, C.-Y.; Lu, X.; Wang, C.-R. *J. Am. Chem. Soc.* **2009**, *131* (46), 16646−16647.
(26) Wu, J.; Wang, T.; Ma, Y.; Jiang, L.; Shu, C.; Wang, C. *J. Phys. Chem. C* **2011**, *115* (48), 23755−23759.
(27) Wang, T.-S.; Feng, L.; Wu, J.-Y.; Xu, W.; Xiang, J.-F.; Tan, K.; Ma, Y.-H.; Zheng, J.-P.; Jiang, L.; Lu, X.; Shu, C.-Y.; Wang, C.-R. *J. Am. Chem. Soc.* **2010**, *132* (46), 16362−16364.
(28) Stevenson, S.; Mackey, M. A.; Stuart, M. A.; Phillips, J. P.; Easterling, M. L.; Chancellor, C. J.; Olmstead, M. M.; Balch, A. L. *J. Am. Chem. Soc.* **2008**, *130* (36), 11844−11845.
(29) Mercado, B. Q.; Olmstead, M. M.; Beavers, C. M.; Easterling, M. L.; Stevenson, S.; Mackey, M. A.; Coumbe, C. E.; Phillips, J. D.; Phillips, J. P.; Poblet, J. M.; Balch, A. L. *Chem. Commun.* **2010**, *46*, 279−281.
(30) Dunsch, L.; Yang, S.; Zhang, L.; Svitova, A.; Oswald, S.; Popov, A. A. *J. Am. Chem. Soc.* **2010**, *132* (15), 5413−5421.
(31) Chen, N.; Chaur, M. N.; Moore, C.; Pinzon, J. R.; Valencia, R.; Rodriguez-Fortea, A.; Poblet, J. M.; Echegoyen, L. *Chem. Commun.* **2010**, *46* (26), 4818−4820.
(32) Valencia, R.; Rodriguez-Fortea, A.; Stevenson, S.; Balch, A. L.; Poblet, J. M. *Inorg. Chem.* **2009**, *48*, 5957−5961.
(33) Popov, A. A.; Dunsch, L. *Chem.—Eur. J.* **2009**, *15* (38), 9707−9729.
(34) Popov, A. A.; Dunsch, L. *J. Phys. Chem. Lett.* **2011**, *2* (7), 786−794.
(35) Popov, A. A.; Chen, C.; Yang, S.; Lipps, F.; Dunsch, L. *ACS Nano* **2010**, *4* (8), 4857−4871.
(36) Zhang, L.; Popov, A. A.; Yang, S.; Klod, S.; Rapta, P.; Dunsch, L. *Phys. Chem. Chem. Phys.* **2010**, *12*, 7840−7847.
(37) Suzuki, T.; Maruyama, Y.; Kato, T.; Kikuchi, K.; Nakao, Y.; Achiba, Y.; Kobayashi, K.; Nagase, S. *Angew. Chem., Int. Ed. Engl.* **1995**, *34* (10), 1094−1096.
(38) Jakes, P.; Dinse, K. P. *J. Am. Chem. Soc.* **2001**, *123* (36), 8854−8855.
(39) Chen, C.; Liu, F.; Li, S.; Wang, N.; Popov, A. A.; Jiao, M.; Wei, T.; Li, Q.; Dunsch, L.; Yang, S. *Inorg. Chem.* **2012**, *51* (5), 3039−3045.
(40) Yang, S.; Popov, A. A.; Dunsch, L. *Angew. Chem., Int. Ed.* **2008**, *47*, 8196−8200.
(41) Miyake, Y.; Suzuki, S.; Kojima, Y.; Kikuchi, K.; Kobayashi, K.; Nagase, S.; Kainosho, M.; Achiba, Y.; Maniwa, Y.; Fisher, K. *J. Phys. Chem.* **1996**, *100*, 9579−9581.
(42) Lu, X.; Nakajima, K.; Iiduka, Y.; Nikawa, H.; Mizorogi, N.; Slanina, Z.; Tsuchiya, T.; Nagase, S.; Akasaka, T. *J. Am. Chem. Soc.* **2011**, *133* (48), 19553−19558.
(43) Kurihara, H.; Lu, X.; Iiduka, Y.; Mizorogi, N.; Slanina, Z.; Tsuchiya, T.; Akasaka, T.; Nagase, S. *J. Am. Chem. Soc.* **2011**, *133* (8), 2382−2385.
(44) Ramsey, N. F. *Phys. Rev.* **1950**, *78* (6), 699−703.
(45) Kurihara, H.; Lu, X.; Iiduka, Y.; Mizorogi, N.; Slanina, Z.; Tsuchiya, T.; Nagase, S.; Akasaka, T. *Chem. Commun.* **2012**, *48*, 1290−1292.
(46) Yang, S.; Popov, A. A.; Chen, C.; Dunsch, L. *J. Phys. Chem. C* **2009**, *113* (18), 7616−7623.
(47) Chen, N.; Beavers, C. M.; Mulet-Gas, M.; Rodriguez-Fortea, A.; Munoz, E. J.; Li, Y.-Y.; Olmstead, M. M.; Balch, A. L.; Poblet, J. M.; Echegoyen, L. *J. Am. Chem. Soc.* **2012**, *134* (18), 7851−7860.
(48) Krause, M.; Kuzmany, H.; Georgi, P.; Dunsch, L.; Vietze, K.; Seifert, G. *J. Chem. Phys.* **2001**, *115* (14), 6596−6605.
(49) Popov, A. A. *J. Comput. Theor. Nanosci.* **2009**, *6* (2), 292−317.
(50) Rivera-Nazario, D. M.; Pinzón, J. R.; Stevenson, S.; Echegoyen, L. A. *J. Phys. Org. Chem.* **2012**, DOI: 10.1002/poc.3009.
(51) Popov, A. A.; Avdoshenko, S. M.; Cuniberti, G.; Dunsch, L. *J. Phys. Chem. Lett.* **2011**, 1592−1600.
(52) Yang, S.; Chen, C.; Popov, A.; Zhang, W.; Liu, F.; Dunsch, L. *Chem. Commun.* **2009**, 6391−6393.
(53) Elliott, B.; Yu, L.; Echegoyen, L. *J. Am. Chem. Soc.* **2005**, *127* (31), 10885−10888.
(54) Yang, S. F.; Zalibera, M.; Rapta, P.; Dunsch, L. *Chem.—Eur. J.* **2006**, *12* (30), 7848−7855.
(55) Pinzon, J. R.; Zuo, T. M.; Echegoyen, L. *Chem.—Eur. J.* **2010**, *16* (16), 4864−4869.
(56) Mercado, B. Q.; Chen, N.; Rodriguez-Fortea, A.; Mackey, M. A.; Stevenson, S.; Echegoyen, L.; Poblet, J. M.; Olmstead, M. M.; Balch, A. L. *J. Am. Chem. Soc.* **2011**, *133* (17), 6752−6760.
(57) Heine, T.; Vietze, K.; Seifert, G. *Magn. Reson. Chem.* **2004**, *42*, S199−S201.
(58) Vietze, K.; Seifert, G. *AIP Conf. Proc.* **2002**, *633* (1), 39−42.
(59) Popov, A. A.; Dunsch, L. *Phys. Chem. Chem. Phys.* **2011**, *13* (19), 8977−8984.
(60) Asher, J. R.; Doltsinis, N. L.; Kaupp, M. *Magn. Reson. Chem.* **2005**, *43* (S1), S237−S247.
(61) Asher, J. R.; Doltsinis, N. L.; Kaupp, M. *J. Am. Chem. Soc.* **2004**, *126* (31), 9854−9861.
(62) Popov, A. A.; Dunsch, L. *J. Am. Chem. Soc.* **2008**, *130* (52), 17726−17742.
(63) Popov, A. A.; Shustova, N. B.; Svitova, A. L.; Mackey, M. A.; Coumbe, C. E.; Phillips, J. P.; Stevenson, S.; Strauss, S. H.; Boltalina, O. V.; Dunsch, L. *Chem.—Eur. J.* **2010**, *16* (16), 4721−4724.
(64) Shustova, N. B.; Peryshkov, D. V.; Kuvychko, I. V.; Chen, Y.-S.; Mackey, M. A.; Coumbe, C. E.; Heaps, D. T.; Confait, B. S.; Heine, T.; Phillips, J. P.; Stevenson, S.; Dunsch, L.; Popov, A. A.; Strauss, S. H.; Boltalina, O. V. *J. Am. Chem. Soc.* **2011**, *133* (8), 2672−2690.
(65) Yannoni, C. S.; Hoinkis, M.; Devries, M. S.; Bethune, D. S.; Salem, J. R.; Crowder, M. S.; Johnson, R. D. *Science* **1992**, *256* (5060), 1191−1192.
(66) Suzuki, S.; Kawata, S.; Shiromaru, H.; Yamauchi, K.; Kikuchi, K.; Kato, T.; Achiba, Y. *J. Phys. Chem.* **1992**, *96* (18), 7159−7161.

(67) Inakuma, M.; Shinohara, H. *J. Phys. Chem. B* **2000**, *104* (32), 7595−7599.
(68) Kato, T. *J. Mol. Struct.* **2007**, *838* (1−3), 84−88.
(69) Wang, T.; Wu, J.; Xu, W.; Xiang, J.; Lu, X.; Li, B.; Jiang, L.; Shu, C.; Wang, C. *Angew. Chem., Int. Ed.* **2010**, *49* (10), 1786−1789.
(70) Wang, T.; Wu, J.; Feng, Y.; Ma, Y.; Jiang, L.; Shu, C.; Wang, C. *Dalton Trans.* **2012**, *41* (9), 2567−2570.
(71) Kurihara, H.; Iiduka, Y.; Rubin, Y.; Waelchli, M.; Mizorogi, N.; Slanina, Z.; Tsuchiya, T.; Nagase, S.; Akasaka, T. *J. Am. Chem. Soc.* **2012**, *134* (9), 4092−4095.
(72) Yang, S. F.; Rapta, P.; Dunsch, L. *Chem. Commun.* **2007**, *2*, 189−191.
(73) Rapta, P.; Popov, A. A.; Yang, S. F.; Dunsch, L. *J. Phys. Chem. A* **2008**, *112*, 5858−5865.
(74) Knight, L. B.; Wise, M. B.; Fisher, T. A. *Inorg. Chem.* **1981**, *20* (8), 2623−2626.
(75) McIntyre, N. S.; Lin, K. C.; Weltner, W. *J. Chem. Phys.* **1972**, *56* (11), 5576−5583.
(76) Weltner, W.; McLeod, D.; Kasai, P. H. *J. Chem. Phys.* **1967**, *46* (8), 3172−3184.
(77) Miliordos, E.; Mavridis, A. *J. Phys. Chem. A* **2010**, *114* (33), 8536−8572.
(78) Kalemos, A.; Kaplan, I. G.; Mavridis, A. *J. Chem. Phys.* **2010**, *132* (2), 024309−7.
(79) Camacho, C.; Witek, H. A.; Cimiraglia, R. *J. Chem. Phys.* **2010**, *132* (24), 244306−9.
(80) Knight, L. B., Jr; Van Zee, R. J.; Weltner, W., Jr. *Chem. Phys. Lett.* **1983**, *94* (3), 296−299.
(81) Knight, L. B.; McKinley, A. J.; Babb, R. M.; Hill, D. W.; Morse, M. D. *J. Chem. Phys.* **1993**, *99* (10), 7376−7383.
(82) Yang, T.; Zhao, X.; Osawa, E. *Chem.—Eur. J.* **2011**, *17* (37), 10230−10234.
(83) Dinse, K. P.; Kato, T. Multi-Frequency EPR Study of Metallo-Endofullerenes. In *Novel NMR and EPR Techniques*; Dolinšek, J., Vilfan, M., Žumer, S., Eds.; Lecture Notes in Physics 684; Springer: Berlin, Heidelberg, 2006; pp 185−207.
(84) Zuo, T.; Xu, L.; Beavers, C. M.; Olmstead, M. M.; Fu, W.; Crawford, T. D.; Balch, A. L.; Dorn, H. C. *J. Am. Chem. Soc.* **2008**, *130* (39), 12992−12997.
(85) Stevenson, S.; Thompson, M. C.; Coumbe, H. L.; Mackey, M. A.; Coumbe, C. E.; Phillips, J. P. *J. Am. Chem. Soc.* **2007**, *129* (51), 16257−16262.
(86) Mercado, B. Q.; Sruart, M. A.; Mackey, M. A.; Pickens, J. E.; Confait, B. S.; Stevenson, S.; Easterling, M. L.; Valencia, R.; Rodriguez-Fortea, A.; Poblet, J. M.; Olmstead, M. M.; Balch, A. L. *J. Am. Chem. Soc.* **2010**, *132*, 12098−12105.
(87) Stevenson, S. Metallic Oxide Clusters in Fullerene Cages. In *Handbook of Carbon Nanomaterials*; D'Souza, F., Kadish, K. M., Eds.; World Scientific Publishing Co.: Singapore, 2011; Vol. *I*, pp 185−205.
(88) Stevenson, S.; Mackey, M. A.; Pickens, J. E.; Stuart, M. A.; Confait, B. S.; Phillips, J. P. *Inorg. Chem.* **2009**, *48* (24), 11685−11690.
(89) Petr, A.; Dunsch, L.; Neudeck, A. *J. Electroanal. Chem.* **1996**, *412* (1, 2), 153−158.
(90) Rapta, P.; Bartl, A.; Gromov, A.; Stasko, A.; Dunsch, L. *ChemPhysChem* **2002**, *3* (4), 351−356.
(91) Stoll, S.; Schweiger, A. *J. Magn. Reson.* **2006**, *178* (1), 42−55.
(92) Perdew, J. P.; Burke, K.; Ernzerhof, M. *Phys. Rev. Lett.* **1996**, *77* (18), 3865−3868.
(93) Laikov, D. N. *Chem. Phys. Lett.* **1997**, *281*, 151−156.
(94) Laikov, D. N.; Ustynuk, Y. A. *Russ. Chem. Bull.* **2005**, *54* (3), 820−826.
(95) Laikov, D. N. *Chem. Phys. Lett.* **2005**, *416* (1−3), 116−120.
(96) Neese, F. *Wiley Interdiscip. Rev.: Comput. Mol. Sci.* **2012**, *2* (1), 73−78.
(97) Neese, F. *ORCA, an ab Initio, Density Functional and Semiempirical Program Package*, version 2.8; Institute for Physical and Theoretical Chemistry: Bonn, Germany, 2010.
(98) Schaefer, A.; Horn, H.; Ahlrichs, R. *J. Chem. Phys.* **1992**, *97* (4), 2571−2577.
(99) Weigend, F.; Ahlrichs, R. *Phys. Chem. Chem. Phys.* **2005**, *7*, 3297−3305.
(100) Neese, F. *Inorg. Chim. Acta* **2002**, *337*, 181−192.
(101) Hedegård, E. D.; Kongsted, J.; Sauer, S. P. A. *Phys. Chem. Chem. Phys.* **2012**, *14*, 10669−10676.
(102) VandeVondele, J.; Krack, M.; Mohamed, F.; Parrinello, M.; Chassaing, T.; Hutter, J. *Comput. Phys. Commun.* **2005**, *167*, 103−128.
(103) The CP2K Developers Group, 2010.
(104) Lippert, G.; Hutter, J.; Parrinello, M. *Theor. Chem. Acc.* **1993**, *103*, 124−140.
(105) Goedecker, S.; Teter, M.; Hutter, J. *Phys. Rev. B* **1996**, *54*, 1703−1710.
(106) Zhurko, G. A. ChemCraft, version 1.6. http://www.chemcraftprog.com, accessed 2011.
(107) Humphrey, W.; Dalke, A.; Schulten, K. *J. Mol. Graphics* **1996**, *14*, 33−38.